Numerical simulation of precipitation kinetics in multicomponent alloys

Xu, K.; Liu, J. D.; van der Zwaag, S.; Xu, W.; Li, J. G.

DOI
10.1016/j.jmst.2022.01.044

Publication date
2022

Document Version
Final published version

Published in
Journal of Materials Science and Technology

Journal of Materials Science & Technology 128 (2022) 98–106

Contents lists available at ScienceDirect

Journal of Materials Science & Technology

journal homepage: www.elsevier.com/locate/jmst

Research Article

Numerical simulation of precipitation kinetics in multicomponent alloys

K. Xu[a], J.D. Liu[b,*], S. van der Zwaag[c], W. Xu[d], J.G. Li[b,*]

[a] School of Materials Science and Engineering, University of Science and Technology of China, Hefei 230026, China
[b] Institute of Metal Research, Chinese Academy of Sciences, Shenyang 110016, China
[c] Novel Aerospace Materials Group, Faculty of Aerospace Engineering, Delft University of Technology, Kluyverweg 1, 2629 HS, Delft, the Netherlands
[d] State Key Laboratory of Rolling and Automation, Northeastern University, Shenyang 110819, China

ARTICLE INFO

Article history:
Received 26 December 2021
Revised 16 January 2022
Accepted 18 January 2022
Available online 10 May 2022

Keywords:
Precipitation kinetics
Thermodynamics
Multicomponent
PSD
Voronoi construction

ABSTRACT

A universal numerical model based on the particle size distribution (PSD) approach has been developed for the simulation of precipitation kinetics in multicomponent alloys during isothermal ageing. Nucleation was implemented utilizing the classical nucleation theory (CNT). Growth and coarsening were modeled by a single growth kinetics equation, which is constructed based on the interfacial diffusion flux balance and the capillarity effect. Only partial off-diagonal terms in the diffusion matrix (diffusion of individual components in the matrix) were taken into account in the calculations to minimize the computational cost while coupling with CALPHAD to extract thermodynamics equilibrium around the interface. A new feature of the model is the incorporation of a more realistic spatial site distribution via a Voronoi construction in the characteristic cell, for the purpose of modifying the diffusion distance. Computational predictions of the precipitate dimensions and the precipitation kinetics were compared with the atom probe tomography (APT) measurements on ternary Ni-Al-Cr alloys isothermally aged at 873 K. It is found that the temporal evolution of the dimensions and composition of the precipitates is well captured, as is the dependence on changes in the alloy composition. The new modification with Voronoi construction demonstrates that the overall precipitation kinetics depends on the density and the spatial site distribution of precipitates. The ability to handle sophisticated alloy chemistries by quantitative equations, the compositional sensitivity of microstructural characteristics emerging from the simulation results, and the ability to visualize the spatial distribution of precipitates make the work very promising for multicomponent alloy design and optimization.

1. Introduction

Accurate and versatile models for the precipitation kinetics in multicomponent metallic alloys are of vital importance for optimizing the composition-microstructure-mechanical properties relationship in commercialized alloys. Various approaches based on the *Ab initio* modelling [1], the phase-field method [2], and the numerical particle size distribution (PSD) approach [3,4] have been applied successfully to capture the precipitation kinetics in multicomponent alloys. Out of the reported models, the PSD approach is the most widely used because it can easily be coupled to CALPHAD-linked thermodynamics databases and is based on solid well-established physical principles. The numerical model in this work is also based on this approach but adds a new topological feature not present in the existing models.

Kampmann and Wagner [5] were the first to propose the PSD model (or Kampmann and Wagner numerical (KWN) model), which relies on the full evolution of particle size distribution and accounts for the simultaneous nucleation, growth, and coarsening of precipitates in dilute binary alloys. In such models, the initial number density and size of the precipitates in each newly created class are computed using classical nucleation theory (CNT). Governed by a growth kinetics equation and accounting for the capillarity effect, the precipitates in PSD classes will grow and shrink depending on their interface curvatures. Later modifications of the growth kinetics equation made the PSD approach applicable to a wide range of multicomponent non-dilute alloy systems including Ni-based alloys, Fe-based alloys, and Al-based alloys [3,6,7]. It has been shown that nucleation, growth, and coarsening regimes emerge naturally without making any arbitrary separation, but fol-

* Corresponding authors at: Institute of Metal Research Chinese Academy of Sciences, China.
E-mail addresses: jdliu@imr.ac.cn (J.D. Liu), jgli@imr.ac.cn (J.G. Li).

https://doi.org/10.1016/j.jmst.2022.01.044
1005-0302/

low from the statistical analysis of the average size, the total number density, and the volume fraction of precipitates over all classes. The PSD implementation can be dealt with in the Lagrange-like or Euler-like approach. The first approach creates number density classes by nucleation and deals with the average size evolution in each class while the second approach predefines the average size classes and deals with number density evolution in each class. The equivalence of both approaches has been demonstrated by Perez et al. [8].

One difficulty in modelling multicomponent precipitation kinetics is to establish a quantitative growth kinetics formulation that is capable of coping with complicated alloy chemistry while keeping a good computational efficiency, especially when the model is coupled with CALPHAD to extract thermodynamics and mobility databases. Chen et al. [9], Rougier et al. [4], and Bonvalet et al. [3] proposed growth rate equations that take into account all off-diagonal terms (i.e., cross-diffusion terms) in the diffusivity matrix. While very accurate, these models are computationally demanding in the case of a high-dimensional diffusivity matrix. In addition, because of the coexistence of positive precipitation and negative precipitation in multicomponent systems [10], it is difficult to characterize the driving force of interface advancement in compositional concentration gradients of individual components directly. Another challenge is associated with the setting of diffusion distance in growth kinetics formulation. Traditionally, this quantitative value is set as its own radius for a specific precipitate class in the PSD approach [3,4,5]. However, due to the effect of spatial site distribution of precipitates on the diffusion kinetics, this simple assumption is not valid in reality.

Considering the aforementioned problems, this work presents a universal multicomponent growth rate equation, which deals with off-diagonal diffusion partially (i.e., diffusion of individual components in the matrix phase) and whose driving force is merely determined by thermodynamics quantities (i.e., compositional concentration and chemical potential distribution in matrix/precipitate) of the diffusion field surrounding the interface while assuming local equilibrium, to maintain computational efficiency and accuracy. Voronoi construction was introduced to picture the spatial distribution of precipitates in a characteristic cell, and then to introduce the diffusion distance in the growth rate equation for each specific precipitate. Firstly, the equation's capability of predicting precipitation pathways in complex multicomponent alloys was demonstrated using the most used Lagrange-like PSD approach. Subsequently, the modified version based on the Voronoi construction was implemented to highlight the importance of modifying local diffusion distances in a controlled manner.

2. Model

2.1. Nucleation equation

The classical nucleation theory (CNT) [11] is taken to calculate the nucleation rate of precipitates, I (m^{-3} s^{-1}):

$$I = N_0\left(1 - f^{\gamma'}\right)Z\beta^* \exp\left(\frac{-\Delta G^*}{k_B T}\right) \tag{1}$$

where N_0 (m^{-3}) is the number density of potential nucleation sites, $f^{\gamma'}$ is the volume fraction of precipitates, Z is the Zeldovich factor that accounts for the decay of partial supercritical clusters, β^* is the condensation rate of solute atoms on a cluster with a critical radius r^* (s^{-1}), ΔG^* is the nucleation barrier (J), k_B is the Boltzmann constant (J K^{-1}), and T is the temperature (K). Assuming a spherical nucleus, Z and β^* can be written as:

$$Z = \frac{V_a \Delta G_V^{\gamma' 2}}{8\pi\sqrt{\sigma^3 k_B T}} \tag{2}$$

$$\beta^* = \frac{4\pi r^*}{a^4}\left(\sum_{i=1}^{C}\frac{1}{D_i x_i^{\gamma}}\right)^{-1} \tag{3}$$

where V_a is the atomic volume (m^3) of matrix and precipitate (assumed to be equal), $\Delta G_V^{\gamma'}$ is the chemical driving force for nucleation or precipitation (J m^{-3}) (and will emerge naturally from growth kinetics equation deduction), π has its usual meaning, σ is the interfacial energy between matrix and precipitate (J m^{-2}), a is the lattice parameter of precipitate (m), and D_i and x_i^{γ} are the diffusion coefficient (m^2 s^{-1}) and atom concentration (at.%) of element i in the matrix. r^* and ΔG^* for nucleation may be written as:

$$r^* = \frac{2\sigma}{\Delta G_V^{\gamma'}} \tag{4}$$

$$\Delta G^* = \frac{16\pi}{3}\frac{\sigma^3}{\Delta G_V^{\gamma' 2}} \tag{5}$$

Nuclei are assumed to be stabilized numerically only beyond the effective radius, r_{eff} (m), which accounts for the size fluctuations of critical clusters [3]:

$$r_{eff} = r^* + \frac{1}{2}\sqrt{\frac{k_B T}{\pi\sigma}} \tag{6}$$

2.2. Growth kinetics equation

The growth rate for a precipitate is controlled by its radius, the degree of supersaturation in the matrix, and the interfacial composition distribution. Following the mean-field approximation, the element concentrations in the matrix are assumed to be uniform. The definition of the diffusion flux used in the present work is inspired by Ref. [12]. Neglecting the concentration gradient in the precipitate itself and assuming that molar volumes of matrix and precipitate are equal, the diffusion flux in the matrix and the flux balance of growing precipitate at the interface for element i could be written separately as:

$$J_i^{\gamma} = -\frac{D_i x_i^{\gamma/\gamma'}}{R_g T V_m^{\gamma'}}\frac{\partial \mu_i^{\gamma}}{\partial r} \tag{7}$$

$$-J_i^{\gamma/\gamma'} = \frac{1}{V_m^{\gamma'}}\frac{dR}{dt}\left(x_i^{\gamma'} - x_i^{\gamma/\gamma'}\right) \tag{8}$$

where $x_i^{\gamma/\gamma'}$ is the atom concentration of element i at the interface, R_g is the gas constant, $V_m^{\gamma'}$ is the molar volume of precipitate, $\partial\mu_i^{\gamma}/\partial r$ is the chemical potential gradient of element i between far-field matrix and interface, ∂r is the diffusion distance, R is the radius of precipitate, dR/dt is the growth rate of precipitate, and $x_i^{\gamma'}$ is the atom concentration of element i in the precipitate. Rearranging Eq. (7), multiplying by $(x_i^{\gamma'} - x_i^{\gamma/\gamma'})$, and summing up to overall element i yields:

$$\sum_{i=1}^{C}\left(\frac{J_i^{\gamma}}{D_i x_i^{\gamma/\gamma'}}R_g T V_m^{\gamma'} + \frac{\partial \mu_i^{\gamma}}{\partial r}\right)\left(x_i^{\gamma'} - x_i^{\gamma/\gamma'}\right) = 0 \tag{9}$$

Assume that $J_i^{\gamma/\gamma'} = J_i^{\gamma}$, and insert Eq. (8) into Eq. (9), then the growth rate is obtained:

$$\frac{dR}{dt} = \frac{\sum_{i=1}^{C}\frac{\partial \mu_i^{\gamma}}{\partial r}\left(x_i^{\gamma'} - x_i^{\gamma/\gamma'}\right)}{\sum_{i=1}^{C}\frac{\left(x_i^{\gamma'} - x_i^{\gamma/\gamma'}\right)^2}{x_i^{\gamma/\gamma'} D_i / R_g T}} \tag{10}$$

Due to the Gibbs–Duhem equation:

$$\sum_{i=1}^{C} \frac{\partial \mu_i^{\gamma}}{\partial r} x_i^{\gamma/\gamma'} = 0 \tag{11}$$

Eq. (10) may be written as:

$$\frac{dR}{dt} = \frac{\sum_{i=1}^{C} \frac{\partial \mu_i^{\gamma}}{\partial r} x_i^{\gamma'}}{\sum_{i=1}^{C} \frac{(x_i^{\gamma'} - x_i^{\gamma/\gamma'})^2}{x_i^{\gamma/\gamma'} D_i / R_g T}} \tag{12}$$

The chemical potential difference between far-field matrix and interface for element ∂i, μ_i^{γ}, is then estimated with the following equation:

$$\partial \mu_i = \bar{\mu}_i^{\gamma} - \mu_{i\,(R)}^{\gamma/\gamma'} \tag{13}$$

where $\bar{\mu}_i^{\gamma}$ and $\mu_{i\,(R)}^{\gamma/\gamma'}$ are the chemical potentials in the far-field matrix (i.e., supersaturation) and at the interface of precipitate with radius R for element i. The modified capillarity effect is introduced to account for the effect of interfacial energy and precipitate size on the interfacial composition:

$$\mu_{i\,(R)}^{\gamma/\gamma'} = \mu_i^{\gamma} + \frac{2\sigma \dot{V}_{\mathrm{m}i}^{\gamma'}}{R} \tag{14}$$

where μ_i^{γ} is the local equilibrium chemical potential of element i near to the interface in the matrix (equal to the equilibrium chemical potential of element i in the precipitate, $\mu_i^{\gamma'}$), $\dot{V}_{\mathrm{m}i}^{\gamma'}$ is the partial molar volume of precipitate and follows the relationship:

$$\sum_{i=1}^{C} x_i^{\gamma'} \dot{V}_{\mathrm{m}i}^{\gamma'} = V_{\mathrm{m}}^{\gamma'} \tag{15}$$

Inserting Eq. (13–15) into Eq. (12), and taking ∂r as precipitate radius R in terms of the traditional way, Eq. (12) may be rewritten as:

$$\frac{dR}{dt} = \frac{\sum_{i=1}^{C} (\bar{\mu}_i^{\gamma} - \mu_i^{\gamma}) x_i^{\gamma'} - \frac{2\sigma V_{\mathrm{m}}^{\gamma'}}{R}}{\sum_{i=1}^{C} \frac{(x_i^{\gamma'} - x_i^{\gamma/\gamma'})^2}{x_i^{\gamma/\gamma'} D_i / R_g T}} \frac{1}{R} \tag{16}$$

Because the chosen strategy in this work is to decompose the precipitation behavior into successive kinetics steps, whose thermodynamics parameters are at local equilibrium near to interface, μ_i^{γ} and $x_i^{\gamma/\gamma'}$ are set as $\mu_i^{\gamma'}$ and x_i^{γ} (local equilibrium atom concentration of element i near to the interface in the matrix), separately. This simplification offers the advantages of higher numerical stability and lower computational cost. Eventually, the growth rate of a precipitate with radius R can be given by:

$$\frac{dR}{dt} = \frac{\sum_{i=1}^{C} (\bar{\mu}_i^{\gamma} - \mu_i^{\gamma'}) x_i^{\gamma'} - \frac{2\sigma V_{\mathrm{m}}^{\gamma'}}{R}}{\sum_{i=1}^{C} \frac{(x_i^{\gamma'} - x_i^{\gamma})^2}{x_i^{\gamma} D_i / R_g T}} \frac{1}{R} \tag{17}$$

The precipitate will grow or shrink accordingly when its R is larger or smaller than the critical radius, R_C, defined by $dR/dt = 0$:

$$R_C = \frac{2\sigma V_{\mathrm{m}}^{\gamma'}}{\sum_{i=1}^{C} (\bar{\mu}_i^{\gamma} - \mu_i^{\gamma'}) x_i^{\gamma'}} \tag{18}$$

One should notice that R_C is equal to the r^* for nucleation, and that $\sum_{i=1}^{C} (\bar{\mu}_i^{\gamma} - \mu_i^{\gamma'}) x_i^{\gamma'} / V_{\mathrm{m}}^{\gamma'}$ is also the $\Delta G_{\mathrm{V}}^{\gamma'}$ for nucleation exactly [13], which means that the model can account for the coexistence of nucleation, growth, and coarsening physically and numerically. Alternatively, Eq. (17) may be written as:

$$\frac{dR}{dt} = \frac{\Delta G_{\mathrm{m}}^{\gamma'} - \frac{2\sigma V_{\mathrm{m}}^{\gamma'}}{R}}{\sum_{i=1}^{C} \frac{(x_i^{\gamma'} - x_i^{\gamma})^2}{x_i^{\gamma} D_i / R_g T}} \frac{1}{R} \tag{19}$$

As shown in Eq. (19), since the competition between the precipitation driving force and the capillarity effect emerges naturally, the model can be also called “competitive growth” [14].

2.3. Lagrange like PSD implementation

At each time step, a new nuclei class, whose number density and critical radius are both a function of the transient matrix supersaturation, is created by the nucleation rate equation (Eq. (1)). The earlier generated classes in the PSD along with the new nuclei class evolve together during the same time step, following the growth rate equation and current matrix supersaturation. If the precipitate size is reduced to zero due to the capillarity effect, the corresponding class will be erased in the PSD. The total number density and the total volume fraction were calculated by summing those of each class, and meanwhile, the average radius and the average concentration in precipitates were calculated by averaging concentrations over all classes in the system. The left matrix supersaturation for element i may be calculated using the mass balance equation:

$$\bar{x}_i^{\gamma} = \frac{x_0^{\gamma} - \bar{x}_i^{\gamma'} f_n^{\gamma'}}{1 - f_n^{\gamma'}} \tag{20}$$

where x_0^{γ} is the initial matrix supersaturation, $\bar{x}_i^{\gamma'}$ is the average atom concentration in precipitates at time step n, and $f_n^{\gamma'}$ is the total volume fraction of precipitates at time step n.

2.4. Modification based on Voronoi construction

The Voronoi construction is taken as a microstructurally defendable optimization strategy to modify the diffusion distance in growth kinetics equation for a specific particle. The whole precipitation kinetics is still divided into multiple time steps. Firstly, the precipitates are confined artificially in a 100 nm × 100 nm × 100 nm characteristic cell in order to keep computational efficiency of building Voronoi cells. The number density and critical radius of precipitates are still determined by the nucleation rate equation (Eq. (1)) based on the volume of characteristic cell, however, the compartmentalization and sites of particle distribution follow the definition of Voronoi construction and meet the criteria that each particle is within one independent Voronoi cell. The specific mathematical procedure is to generate the coordinates of particles randomly, and meanwhile make sure that, for any two particles in PSD of the characteristic cell, their radii are smaller than the half of the center to center distance. The integral Voronoi cells can thus be constructed graphically according to the coordinate array of PSD in the characteristic cell, using Multi-Parametric Toolbox in Matlab environment [15]. The diffusion field of each particle is seen within the corresponding Voronoi cell at each time step. The diffusion distance for one specific particle could be thus set as R_{V} - R (R_{V} is the average distance between the center and vertices in one Voronoi cell, and R is the radius of particle). It should be emphasized that, unlike the appraoch in the Lagrange-like PSD implementation, each particle is assumed to be one class under this case and will evolve separately at each time step, according to its own size and diffusion distance. However, the statistical computation of the dimensional properties of entire precipitates, the compositional properties in precipitates and the left matrix supersaturation is still based on methods in section *2.3*. When each new time step starts, the spatial distribution of precipitates and the Voronoi construction in the characteristic cell will be reconstructed in order to demonstrate randomness. Thermodynamics quantities emerged in the growth rate equation are extracted by coupling with the TQ-interface in Thermo-Calc. The framework is written in Fortran environment. The construction of Voronoi cells are achieved through

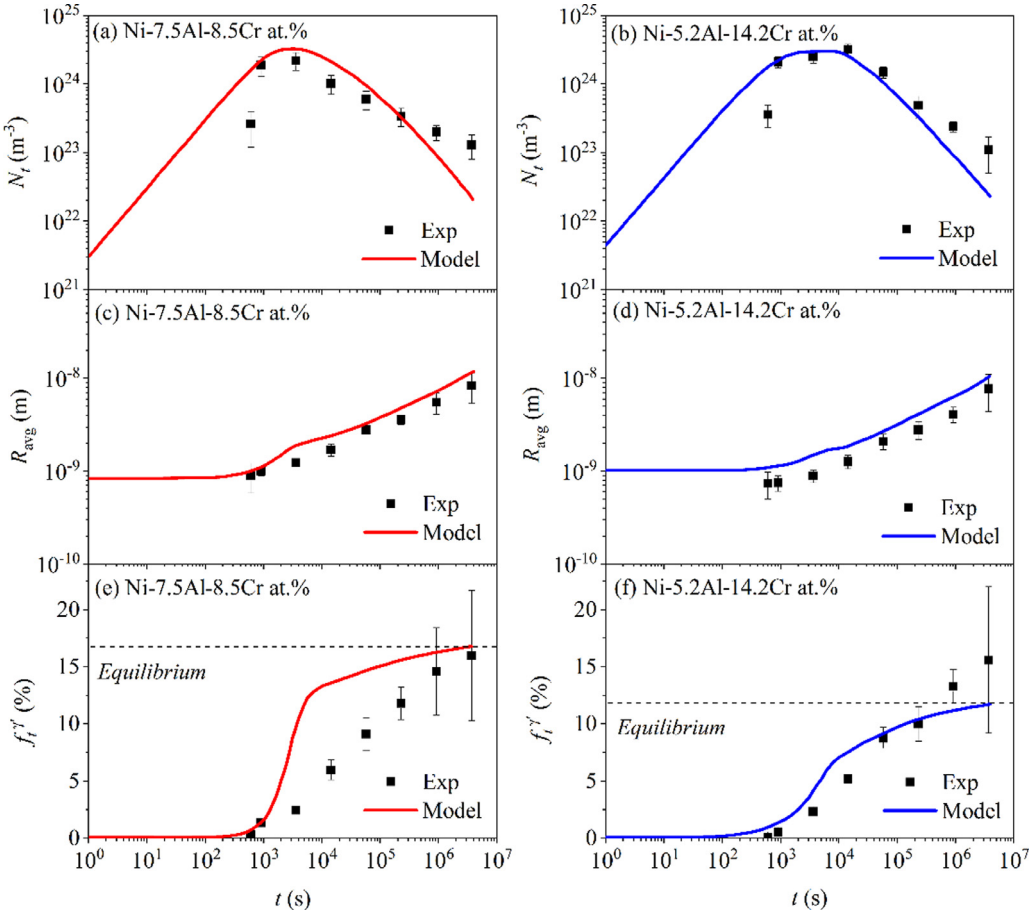

Fig. 1. Temporal evolution of (a) and (b) number density, N_t, (c) and (d) average radius, R_{avg}, and (e) and (f) volume fraction, $f_t^{\gamma'}$, of γ' precipitates in alloys (A) Ni-7.5Al-8.5Cr at.% and (B) Ni-5.2Al-14.2Cr at.% at 873 K isothermal ageing. The black dots correspond to the experimental data of Booth-Morrison et al. [16].

Table 1
Input parameters for alloys (A) Ni-7.5Al-8.5Cr at.% and (B) Ni-5.2Al-14.2Cr at.%.

	N_0 (m^{-3})	σ (mJ m^{-2})	V_a (m^3)	$V_m^{\gamma'}$ (m^3 mol^{-1})	a (m)
(A)	3×10^{27}	28.5	1.09×10^{-29}	6.59×10^{-6}	3.4×10^{-10}
(B)	8×10^{27}	30	1.09×10^{-29}	6.59×10^{-6}	3.4×10^{-10}

the hybrid programming of Multi-Parametric Toolbox of Matlab in the Fortran framework.

3. Results and discussion

3.1. Capability of numerical model

To demonstrate the capability of the model, the kinetics equations in sections 2.1 and 2.2 were applied to simulating the temporal evolution of the dimensional and compositional properties of the precipitates in a set of ternary Ni-Al-Cr alloys during 1024 h isothermal ageing at 873 K. The experimental data for validation were extracted from two-atom probe tomography (APT) studies performed by either Booth-Morrison et al. [16] or Mao et al. [17]. It is noteworthy that the morphology of γ' precipitates are irregular and quasi-spherical in these two Ni-Al-Cr alloys, so we assume the isotropic scenario and ignore the effect of mismatch strain field between γ and γ' on the morphology transformation from spherical to cuboidal, which is common in the complicated Ni-based superalloys. Initially, the alloys were assumed to be fully austenitic without any γ' precipitates. The potential nucleation site density N_0 for homogeneous nucleation theory and the interfacial energy σ are taken as fitting parameters so that to get the best fitting results for the two alloys in this work. The actual values for the two alloys are listed in Table 1. Subsequently, a sensitivity analysis of compositional changes in the temporal evolution of dimensional properties was presented to demonstrate the prospect of applying the model for compositional optimization of multicomponent alloys.

3.1.1. Temporal evolution of dimensional and compositional properties

As shown in Fig. 1, it is found that the simulated temporal evolution of N_t, R_{avg}, and $f_t^{\gamma'}$ during 1024 h isothermal ageing at 873 K fits well the APT data for alloys (A) Ni-7.5Al-8.5Cr at.% and (B) Ni-5.2Al-14.2Cr at.%. Owing to the similarity of the evolutional features of N_t, R_{avg}, and $f_t^{\gamma'}$, in both alloys, the simulation results will only be discussed in detail for alloy (A) Ni-7.5Al-8.5Cr at.%. Naturally, the overall precipitation kinetics can be divided into three regimes showing the typical characteristics of nucleation, growth, and coarsening, without making arbitrary separations. During the first regime corresponding to the nucleation of γ' precipitates ($t <$ 500 s), the number density increases dramatically, whilst the average radius and the total volume fraction remain close to zero because of the tiny size of the precipitates. As shown in Fig. 1 (a), in the time interval $500 < t < 10^4$ s, the nucleation rate diminishes gradually until the maximum number density is reached, indicating that the matrix supersaturation has nearly come to an end due to the massive precipitation of γ' precipitates during this period. Fig. 1(c, e) shows that the average radius and the total volume fraction of precipitates increase concurrently because the

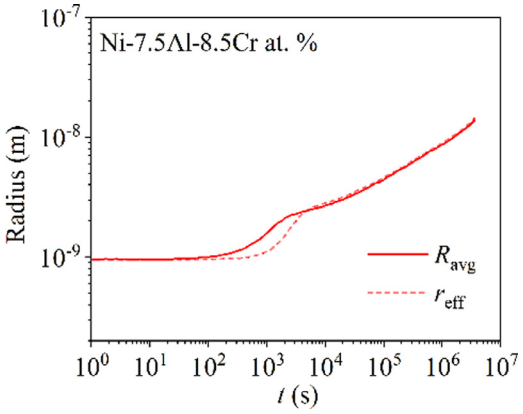

Fig. 2. Temporal evolution of the relationship between average radius, R_{avg}, and effective radius, r_{eff} (which can be seen equally as critical radius, r^*), in the alloy (A) Ni-7.5Al-8.5Cr at.% at 873 K isothermal ageing.

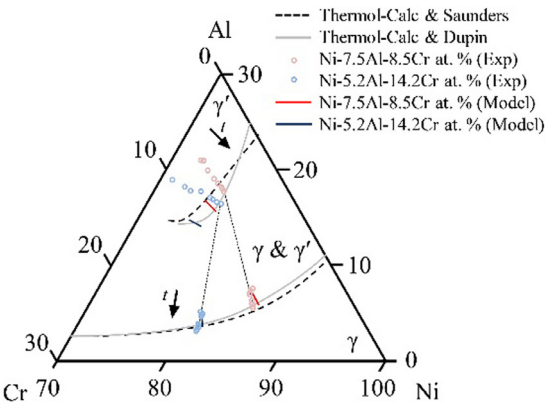

Fig. 4. Compositional trajectories of γ matrix and γ' phase for alloys (A) Ni-7.5Al-8.5Cr at.% (red line) and (B) Ni-5.2Al-14.2Cr at.% (blue line) during isothermal ageing, in a partial Ni-Al-Cr ternary phase diagram at 873K, calculated by Thermo-Calc, employing the TCNi8 database. Two types of drawn equilibrium solvus curves are determined by Thermo-Calc utilizing databases from Saunders [28] (black dash line) and Dupin and Sundman [29] (gray line), respectively. The experimental APT data of compositional evolution in the γ matrix and γ' phase for alloys (A) Ni-7.5Al-8.5Cr at.% (open red circles) and (B) Ni-5.2Al-14.2Cr at.% (open blue circles) are extracted from the work of Booth-Morrison et al. [16].

diffusion-controlled growth becomes dominant. As the matrix supersaturation continues to decrease, the capillarity effect will have a larger effect on the evolution of number density, average radius, and volume fraction of γ' precipitates. The appearance of coarsening characteristics can be better recognized from the evolution of the relationship between R_{avg} and r_{eff} displayed in Fig. 2. After about 10^4 s, the value of r_{eff} starts to exceed that of R_{avg} but in a gentle way until these two values become almost equal. This result indicates that the sizes of quite a few precipitate classes are lower than the critical radius during this regime, and thus, quantities of relatively smaller precipitates are shrinking accompanied by the growth of larger precipitates, i.e., larger precipitates grow at the expense of smaller ones. The time dependencies of N_t and R_{avg} in alloy (A) Ni-7.5Al-8.5Cr at.% after 10^4 s are illustrated further by dotted curves in Fig. 3. Evidently, the alloy system is in the quasi-stationary stage after long-time ageing and follows the classical Lifshitz and Slyozov, Wagner (LSW) theory (i.e. $N_t^{-1} \sim t$ and $R_{avg}^3 \sim t$) [18], which means that coarsening has become the dominant process.

One can also note that $f_t^{\gamma'}$ still keeps increasing at a very slow rate after 10^4 s, then the equilibrium value is reached according to Fig. 1(e, f). This phenomenon indicates that coarsening is not the only mechanism functioning here. As a matter of fact, because of the effect of residual supersaturation in the matrix, the fresh γ' phase is still precipitating after 10^4 s by the overlap between growth and coarsening [4,19]. The traditional viewpoint about explicit isolation between growth and coarsening is not fully appropriate in this case. Indeed, the foundation of LSW theory is based on the assumption of an ideal dilute solution (i.e. the effect of volume fraction is not incorporated) and thus is more suitable for the pure equilibrium state [18,20,21].

Fig. 4 shows the comparison between simulated compositional trajectories of the γ matrix and the γ' phase and the measured one during 1024 h isothermal ageing at 873 K in alloys (A) Ni-7.5Al-8.5Cr at.% and (B) Ni-5.2Al-14.2Cr at.%. It is clear that the compositional evolution of the γ matrix is well predicted by the numerical model as the final concentrations lie on the equilibrium solvus values, whereas the simulated compositional evolution in the γ' phase does not superimpose exactly with the measured one. The reason why this occurs is that the simulated compositional evolution in the γ' phase and final equilibrium composition of the γ' phase are mainly determined by the accuracy of the thermodynamics database (i.e., equilibrium composition prediction in the γ' phase under different supersaturation), owing to the local equilibrium assumption used for diffusion field and the method of decomposing overall precipitation into equilibrium kinetics steps. Nevertheless, the compositional evolution in the γ matrix (i.e. overall precipitation kinetics) can be easily controlled by adjusting parameters like N_0 and σ in the numerical model [22,23], in spite of the thermodynamics database shortcomings. The specific tem-

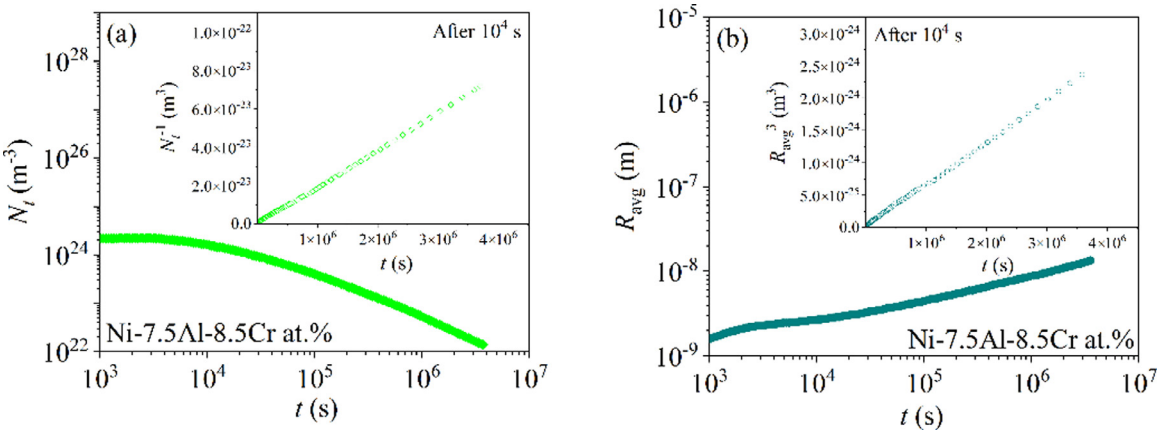

Fig. 3. Time dependencies of (a) number density, N_t, and (b) average radius, R_{avg}, in alloy (A) Ni-7.5Al-8.5Cr at.% at 873 K isothermal ageing, after 10^4 s.

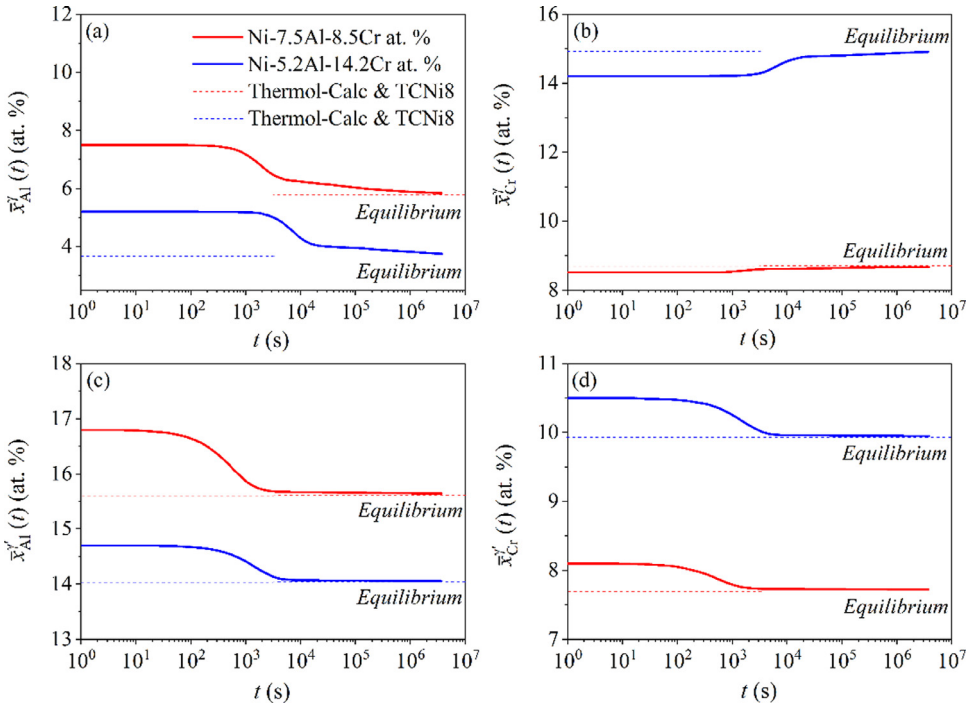

Fig. 5. Temporal evolution of compositions in γ matrix and γ' phase for alloys (A) Ni-7.5Al-8.5Cr at.% (red line) and (B) Ni-5.2Al-14.2Cr at.% (blue line) at 873 K isothermal ageing. The equilibrium compositions at 873K for alloys (A) Ni-7.5Al-8.5Cr at.% (red short dash line) and (B) Ni-5.2Al-14.2Cr at.% (blue short dash line) are calculated by Thermo-Calc and TCNi8 database.

poral evolution of compositions in the γ matrix and γ' phase for alloys (A) Ni-7.5Al-8.5Cr at. % and (B) Ni-5.2Al-14.2Cr at. % during 1024 h isothermal ageing at 873 K is shown in Fig. 5. As shown in Fig. 5 (a, b), compositions in the γ matrix evolve from the nominal alloy compositions to the equilibrium values given by Thermo-Calc and TCNi8 database. However, for the temporal evolution of compositions in the γ' phase in Fig. 5 (c, d), the initial setting of critical nucleus compositions during nucleation would also significantly influence the trend and values of compositional evolution. The critical nucleus composition is reported to be related to the preferential segregation in the cluster, the chemical fluctuation in the matrix, and the internal stress [24,25,26,27], which are difficult to calculate by CALPHAD. Here, to satisfy the compositional evolution trend measured by Booth-Morrison et al. [16] (i.e., compositions of Al and Cr in the γ' phase decrease with time), the γ' phase compositions that can give one of the maximum precipitation driving force values and meanwhile are higher than the equilibrium values are taken as the critical nucleus compositions in this work for two alloys. Although simulated compositional trajectories of the γ' phase deviate slightly from the experimental one numerically in Fig. 4, the overall compositional evolution trend of the γ matrix and γ' phase in Fig. 5 fits the measurement of Booth-Morrison et al. [16] rather well.

Compared with the temporal evolution of dimensional properties shown in Fig. 1, a high synchronization of the temporal evolution of compositional properties is achieved as shown in Fig. 5. For alloy (A) Ni-7.5Al-8.5Cr at.%, the compositions in the γ matrix and γ' phase during the nucleation regime ($t < 500$ s) are the nominal alloy compositions and the calculated critical nucleus compositions, respectively. When growth regime ($500 < t < 10^4$ s) occurs, conspicuous compositional evolution in both γ matrix and γ' phase is observed because of the extensive precipitation of γ' precipitates. After that ($t > 10^4$ s), as reflected in the slight changes in volume fraction shown in Fig. 1(e), the compositions in the γ matrix and γ' phase still evolve at a very low rate until the equilibrium states are reached. This phenomenon indicates that the γ'

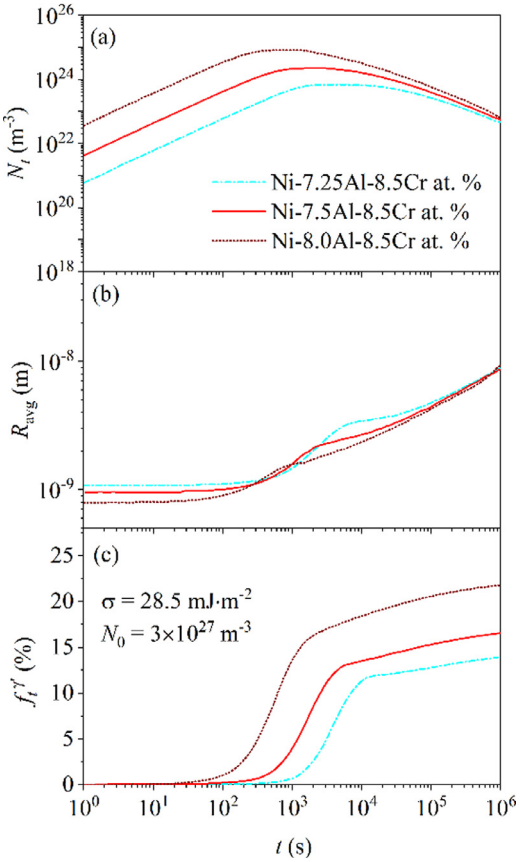

Fig. 6. Influence of compositional variation of Al on (a) number density, N_t, (b) average radius, R_{avg}, and (c) volume fraction, $f_t^{\gamma'}$, of γ' precipitates as a function of time in the alloy (A) Ni-7.5Al-8.5Cr at. % at 873 K isothermal ageing.

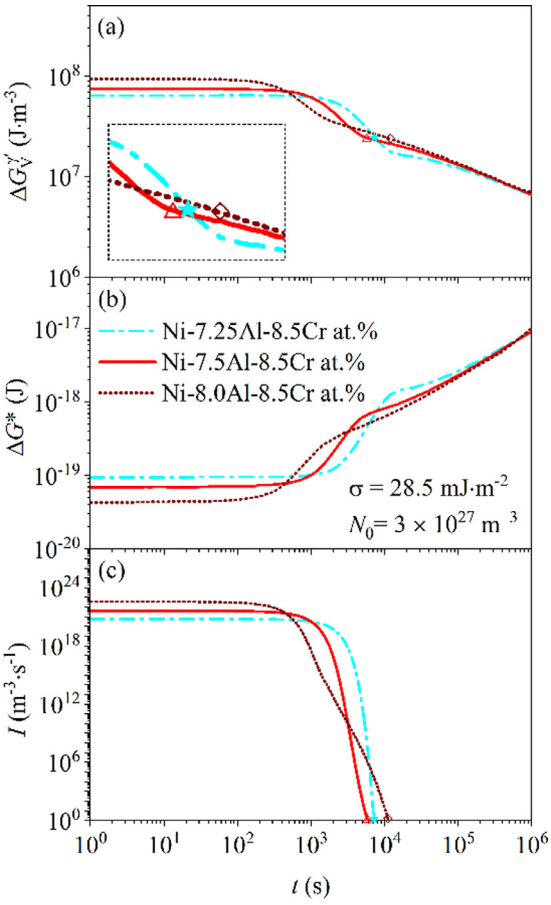

Fig. 7. Influence of compositional variation of Al on (a) chemical driving force for precipitation, $\Delta G_V^{\gamma'}$, (b) nucleation barrier, ΔG^*, and (c) nucleation rate, I, of γ' precipitates as a function of time in the alloy (A) Ni-7.5Al-8.5Cr at.% at 873 K isothermal ageing. The inserted zoom shows the time points when nucleation finish and their positions on chemical driving force curves, for different Al content.

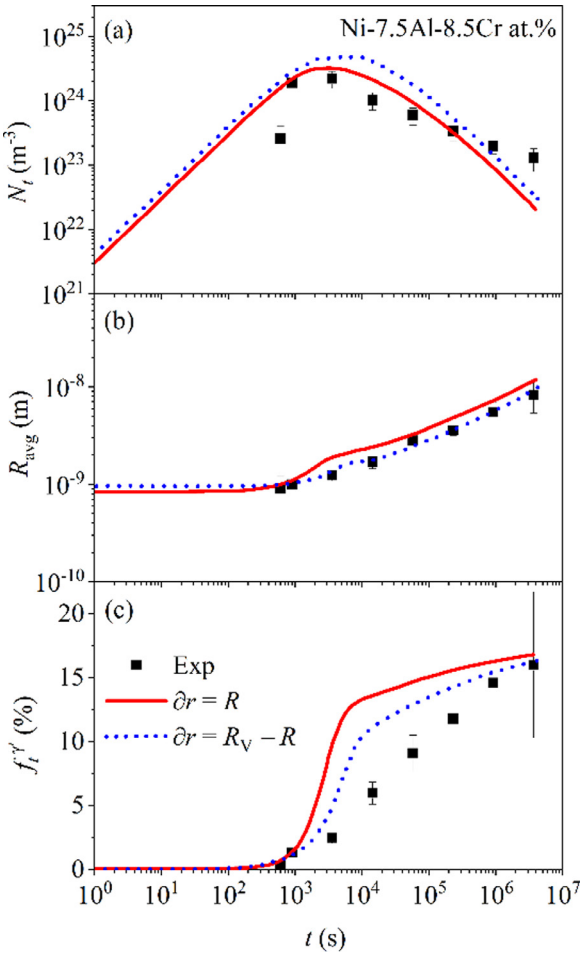

Fig. 8. Influence of modifying diffusion distance on (a) number density, N_t, (b) average radius, R_{avg}, and (c) volume fraction, $f_t^{\gamma'}$, of γ' precipitates as a function of time in the alloy (A) Ni-7.5Al-8.5Cr at.% at 873 K isothermal ageing (traditional diffusion distance setting, $\partial r = R$: red lines, modified diffusion distance, $\partial r = R_V - R$: blue short dot lines).

phase is still precipitating, corresponding to the overlap between growth and coarsening that we mentioned above.

3.1.2. Sensitivity analysis of compositional variation

A plot of the simulated dimensional properties evolution as a function of the change in Al concentration for alloy (A) Ni-7.5Al-8.5Cr at.% at 873 K isothermal ageing is shown in Fig. 6. As expected, as the Al content increases, the overall precipitation kinetics is accelerated. For a higher Al content, a higher number density and a smaller average radius during the nucleation regime are shown in Fig. 6(a, b), respectively. Fig. 6(c) illustrates that the predicted volume fraction of γ' precipitates is elevated because of the overall increment in supersaturation in the γ matrix, and as a result, the increase of volume fraction of γ' precipitates is brought forward as well. To better explain these characteristics above, it is useful to primarily consider the effect of changes in the Al concentration on the evolution of $\Delta G_V^{\gamma'}$ (the overall supersaturation in the γ matrix) of γ' precipitates during the precipitation process, i.e., Fig. 7(a). For the case of the higher Al content, the smaller average radius during the nucleation regime can be easily understood by the numerical relationship shown in Eq. (4), because the initial $\Delta G_V^{\gamma'}$ is raised by the increment of Al content in the ternary Ni-Al-Cr alloy system, as shown in Fig. 7(a). The appearance of higher number density during the nucleation regime can thus be ascribed to the variation of nucleation rate correspondingly. According to the internal correlation between Eqs. (1) and (5), if the $\Delta G_V^{\gamma'}$ is raised, the ΔG^* will be decreased (which can also be seen in Fig. 7(b)), and hence the nucleation rate will be increased. In addition to the change of nucleation kinetics, a faster growth rate equation, i.e., Eq. (19), can also be acquired through the higher initial $\Delta G_V^{\gamma'}$, therefore speeding up the increment of volume fraction of γ' precipitates shown in Fig. 6(c) and the decrease of $\Delta G_V^{\gamma'}$ (the depletion of supersaturation in the γ matrix) in Fig. 7(a).

For the case of the lower Al content, i.e., alloy Ni-7.25Al-8.5Cr at.%, there are pronounced plateaus in the number density and the average radius of about 7000 s, as shown in Fig. 6(a, b), indicating that there is a gap between the termination of nucleation and the onset of coarsening. As shown in the inserted zoom in Fig. 7(a), the time point when nucleation stops lies within the stage in which the $\Delta G_V^{\gamma'}$ curve has not turned obviously into coarsening for alloy Ni-7.25Al-8.5Cr at.%. This means that nucleation has terminated before the massive coarsening becomes dominant, therefore showing the interim period accompanied by the number density plateau [23]. The average radius plateau can therefore be explained as a numerical issue that the growth of large particles compensates for and even exceeds the shrinkage of small particles while the small particles are not fully dissolved.

3.2. Importance of modifying diffusion distance

The influence of modifying the local diffusion distance with the Voronoi construction on the temporal evolution of N_t, R_{avg}, and $f_t^{\gamma'}$ in the alloy (A) Ni-7.5Al-8.5Cr at.% at 873 K isothermal ageing is il-

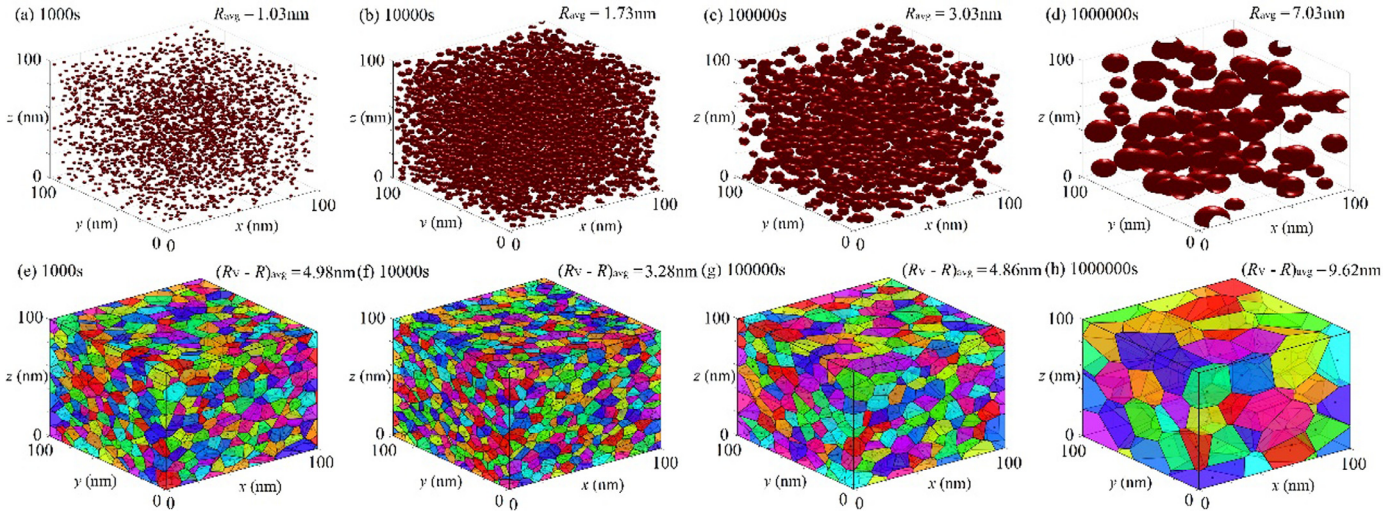

Fig. 9. Spatial distribution of precipitates and Voronoi cells within a 100 nm × 100 nm × 100 nm characteristic cell at different time points in the alloy (A) Ni-7.5Al-8.5Cr at.% at 873 K isothermal ageing (the compartmentalization of particle distribution can meet the criteria that each particle is within one Voronoi cell).

lustrated in Fig. 8. It is worth noting that the kinetics steps are set short enough to keep precipitates from growing beyond corresponding Voronoi cells. So, interactions among neighboring particles are ignored here. Compared with simulated results based on traditional diffusion distance setting ($\partial r = R$), the simulated precipitation pathways ($\partial r = R_V - R$) fit better with the APT experimental data, especially for the evolution of R_{avg} and $f_t^{\gamma'}$ shown in Fig. 8(b, c). As a matter of fact, due to the influence of modified non-equal diffusion distance on the growth kinetics equation, the overall precipitation kinetics decelerates. This can be understood qualitatively as follows. As shown in Fig. 9, the average modified diffusion distance, $(R_V - R)_{avg}$, is much higher than the average traditional diffusion distance, R_{avg}, during the overall precipitation process. Consequently, the growth rate is reduced, leading to lower values for R_{avg} and $f_t^{\gamma'}$. The higher N_t can thus be ascribed to the higher nucleation kinetics induced by the higher degree of supersaturation in the matrix. It is also worth mentioning that the average diffusion distance given by the Voronoi construction is in accordance with the reported fact that Al is not likely to diffuse more than 10 nm in the γ matrix when annealing below 873 K [30].

One possible source of error between the simulation and the experiment is the local equilibrium assumption used for the diffusion field, which does not take into account soft impingement (the overlap of diffusion fields of neighboring precipitates) [31,32], hard impingement (the coalescence or coagulation caused by direct contacts between precipitates) [33,34], and the physical geometry (shape anisotropy) [35]. Apart from blaming the simplifications in the model, another possible error source may be ascribed to the uncertainties in APT experiments, especially for the volume fraction measurement at longer time ageing. Indeed, as we can see in Fig. 8(b), the size of measured γ' precipitates has been very close to the sectional area of conventional APT analysis after 10^6 s [16,36]. In spite of these limitations above, the overall precipitation kinetics (the temporal evolution of number density, average radius, and volume fraction of γ' precipitates) are well predicted.

4. Conclusions

A successful universal multicomponent precipitation kinetics model, based on the classical KWN model and highly coupled with CALPHAD, was proposed. The growth kinetics equation which only incorporates partial off-diagonal diffusion (diffusion of individual components in the matrix) shows very good computational efficiency and accuracy when predicting the temporal evolution of dimensional and compositional properties of multicomponent alloys during isothermal ageing. Voronoi construction is taken as a new optimization to picture the spatial distribution of precipitates and modify the local diffusion distance. It is shown that the simulation with modified diffusion distance fits the experimental APT data better. More importantly, the low computational cost reflected from simple kinetics equations, the compositional sensitivity of microstructural characteristics, and the visualization of the spatial distribution of precipitates may highlight the models' capability in the area of materials optimization and design. The source code and instruction are available at http://github.com/KeXuMSE/Voronoi-Construction-based-Kampmann-and-Wagner-numerical-model.

Conflict of Interest

All of the authors declare no conflict of interests.

Acknowledgements

This work was financially supported by the National Natural Science Foundation of China (No. 51871221), the National Key R&D Program of China (No. 2020YFA0714900), and the National Science and Technology Major Project (J2019-VI-0023-0139 and J2019-VII-0004-0144).

References

[1] D. Giofré, T. Junge, W.A. Curtin, M. Ceriotti, Acta Mater. 140 (2017) 240–249.
[2] M.S. Bhaskar, Comput. Mater. Sci. 146 (2018) 102–111.
[3] M. Bonvalet, T. Philippe, X. Sauvage, D. Blavette, Acta Mater. 100 (2015) 169–177.
[4] L. Rougier, A. Jacot, C.A. Gandin, P.D. Napoli, P.Y. Théry, D. Ponsen, V. Jaquet, Acta Mater. 61 (2013) 6396–6405.
[5] R. Kampmann, R. Wagner, in: P. Haasen, V. Gerold, R. Wagner (Eds.), Decomposition of Alloys: The Early Stages, Pergamon Press, Oxford, 1984, pp. 91–103.
[6] H. Guo, M. Enomoto, C.J. Shang, Comput. Mater. Sci. 141 (2018) 101–113.
[7] Q. Du, K. Tang, C.D. Marioara, S.J. Andersen, B. Holmedal, R. Holmestad, Acta Mater. 122 (2017) 178–186.
[8] M. Perez, M. Dumont, D. Acevedo-Reyes, Acta Mater. 56 (2008) 2119–2132.
[9] Q. Chen, J. Jeppsson, J. Ågren, Acta Mater. 56 (2008) 1890–1896.
[10] C. Zener, J. Appl. Phys. 20 (1949) 950–953.
[11] C.N. Nanev, Theory of Nucleatio, Handbook of Crystal Growth, Second Edition, Elsevier, Boston, 2015.
[12] J. Ågren, M.T. Mora, G.Inden J.Golcheski, H. Kumar, C. Sigli, Calphad-Comput. Coupling Ph. Diagrams Thermochem. 24 (2000) 41–54.
[13] D.A. Porter, K.E. Easterling, Phase Transformations in Metals and Alloys (revised reprint), Chemical Rubber Company Press, Florida, 2009.

[14] A. Azzam, T. Philippe, A. Hauet, F. Danoix, D. Locq, P. Caron, D. Blavette, Acta Mater. 145 (2018) 377–387.
[15] M. Kvasnica, P. Grieder, M. Baotic, M. Morari, 2004.
[16] C. Booth-Morrison, J. Weninger, C.K. Sudbrack, Z. Mao, R.D. Noebe, D.N. Seidman, Acta Mater. 56 (2008) 3422–3438.
[17] Z.G. Mao, C. Booth-Morrison, C.K. Sudbrack, G. Martin, D.N. Seidman, Acta Mater. 60 (2012) 1871–1888.
[18] I.M. Lifshitz, V.V. Slyozov, J. Phys. Chem. Solids 19 (1961) 35–50.
[19] S. Bahl, L. Xiong, L.F. Allard, R.A. Michi, J.D. Poplawsky, A.C. Chuang, D. Singh, T.R. Watkins, D. Shin, J.A. Haynes, A. Shyam, Mater. Des. 198 (2021) 109378.
[20] C.K.L. Davies, P. Nash, R.N. Stevens, Acta Metall. 28 (1980) 179–189.
[21] J. Svoboda, F.D. Fischer, Acta Mater. 79 (2014) 304–314.
[22] Q. Zhang, S.K. Makineni, J.E. Allison, J.C. Zhao, Scr. Mater. 160 (2019) 70–74.
[23] J.D. Robson, Modelling the overlap of nucleation, Acta Mater. 52 (2004) 4669–4676.
[24] W.E. Frazier, T.G. Lach, T.S. Byun, Acta Mater 194 (2020) 1–12.
[25] M. Wang, S. Guo, X. Lin, W.D. Huang, Mater. Lett. 285 (2021) 129206.
[26] J. Ženíšek, E. Kozeschnik, J. Svoboda, F.D. Fischer, Acta Mater. 91 (2015) 365–376.
[27] J. Zhu, T. Zhang, Y. Yang, C.T. Liu, Acta Mater. 166 (2019) 560–571.
[28] N. Saunders, 8th International Symposium on Superalloys, Champion, PA, September 22–26, 1996.
[29] N. Dupin, B. Sundman, Scand. J. Metall. 30 (2001) 184–192.
[30] Y.Q. Chen, E. Francis, J. Robson, M. Preuss, S.J. Haigh, Acta Mater. 85 (2015) 199–206.
[31] C. Ioannidou, Z. Arechabaleta, A. Navarro-López, A. Rijkenberg, R.M. Dalgliesh, S. Kölling, V. Bliznuk, C. Pappas, J. Sietsma, A.A. van Well, S.E. Offerman, Acta Mater. 181 (2019) 10–24.
[32] A. Miotti Bettanini, L. Ding, J.D. Mithieux, C. Parrens, H. Idrissi, D. Schryvers, L. Delannay, T. Pardoen, P.J. Jacques, Mater. Des. 162 (2019) 362–374.
[33] F. Masoumi, M. Jahazi, D. Shahriari, J. Cormier, J. Alloy. Compd. 658 (2016) 981–995.
[34] J.C. Zhang, L. Liu, T.W. Huang, J. Chen, K.L. Cao, X.X. Liu, J. Zhang, H.Z. Fu, J. Mater. Sci. Technol. 62 (2021) 1–10.
[35] K. Kim, P.W. Voorhees, Acta Mater. 152 (2018) 327–337.
[36] R. Hu, S.B. Jin, G. Sha, Prog. Mater. Sci. (2020) 100740.